RSC Applied Interfaces

ROYAL SOCIETY OF CHEMISTRY

PAPER

View Article Online
View Journal

Cite this: DOI: 10.1039/d6lf00079g

Electrocatalytic characteristics of $Cu_{0.95}Co_{2.05}O_4/MoO_3$/NF with a heterojunction for pyrazine hydrogenation

Xin Zheng,[a] Yajie Zhang,[b] Hanyu Li,[a] Fangcheng Qiu,[a] Siyi Chen[b] and Shengping Wang *[b]

Electrocatalytic hydrogenation of N-heterocyclic compounds using water as the hydrogen source under mild conditions offers a promising route for liquid organic hydrogen carrier (LOHC) storage, yet achieving both high activity and selectivity with non-precious metal catalysts remains challenging. In this study, we developed a self-supported $Cu_{0.95}Co_{2.05}O_4/MoO_3$/NF heterojunction electrocatalyst that enables efficient pyrazine hydrogenation to piperazine. The heterointerface creates a strong built-in electric field, which drives directional electron transfer from MoO_3 to $Cu_{0.95}Co_{2.05}O_4$. This electronic redistribution renders Cu sites that are electron-rich for selective pyrazine adsorption/hydrogenation, whereas Mo and Co sites become electron-deficient to promote water dissociation and active hydrogen (H*) generation. The spatially adjacent sites work synergistically *via* a surface spillover mechanism, suppressing the competing hydrogen evolution reaction. As a result, the catalyst delivers a pyrazine conversion >95% and a piperazine selectivity >80% after 1.5 h at −0.25 V *vs.* RHE in alkaline medium, with excellent cycling stability. This work demonstrates that interfacial electronic engineering of non-noble metal heterostructures provides a viable strategy for mild, low-cost LOHC hydrogenation.

Received 10th March 2026,
Accepted 22nd May 2026

DOI: 10.1039/d6lf00079g

rsc.li/RSCApplInter

1 Introduction

To address the growing challenges of the energy crisis, environmental pollution, and fossil fuel depletion, developing new renewable energy sources is crucial.[1–3] Hydrogen energy, a clean and efficient renewable resource, is pivotal for energy transition. However, its low density and safety concerns limit large-scale storage.[4,5] For efficient hydrogen storage, researchers have developed various technologies, including high-pressure gaseous storage, cryogenic liquid storage, solid-state materials, and liquid-phase chemical hydrogen storage materials.[6–9]

Among these methods, electrochemical water splitting has emerged as a promising route for green hydrogen production, with recent efforts focusing on developing efficient electrocatalysts for both the hydrogen evolution reaction (HER) and the oxygen evolution reaction (OER) using transition metal-based materials.[10,11] Moreover, achieving industrial-scale current density remains a key challenge, and advanced strategies such as 3D substrate integration and binder-free synthesis have been proposed to enhance electrochemical performance.[12] Liquid-phase chemical hydrogen storage materials function by bonding hydrogen atoms to hydrogen-lean molecules in liquid compounds. They offer simple operation, moderate mass density, and good stability at room temperature.[13,14] On the basis of the origin of the hydrogen-lean molecule, these materials can be classified into CO_2-derived systems and liquid organic hydrogen carriers (LOHCs). LOHCs have attracted significant attention because of their reversible hydrogenation–dehydrogenation cycles.[15] Recent studies have further demonstrated that the electrocatalytic hydrogenation of aromatic LOHCs offers significant advantages because it eliminates the use of gaseous hydrogen and enables safer, more energy-efficient production.[16] Among LOHCs, N-heterocyclic aromatic compounds (*e.g.*, *N*-ethylcarbazole and quinoline) are particularly promising, as their performance surpasses that of traditional benzene-based systems.[17–20]

Nevertheless, their conventional hydrogenation/dehydrogenation processes require high temperatures and precious metal catalysts. This leads to high costs and hinders large-scale application.[21] Electrocatalytic hydrogenation (ECH) presents a unique advantage in overcoming this bottleneck. This process operates under ambient conditions and uses water as the *in situ* hydrogen source. This approach avoids the need for external high-pressure H_2 and precious

[a] *Electric Power Research Institute, Yunnan Power Grid Co Ltd, Kunming 650220, China*
[b] *Faculty of Material Science and Chemistry, China University of Geosciences, Wuhan 430074, China. E-mail: spwang@cug.edu.cn*

metal catalysts.[22] For example, water has been used as the hydrogen source for the electrochemical semihydrogenation of alkynols,[23] with 2-methyl-3-butyn-2-ol as the model substrate, and both the conversion and selectivity were simultaneously improved. Site-selective electroreductive hydrogenation of benzylic olefins using water as the hydrogen donor has been reported.[24] These works confirm that electrocatalytic systems enable efficient and highly selective hydrogenation of organic molecules, offering a promising solution for the mild, safe, and low-cost conversion of LOHCs. For example, Guo *et al.* reported the use of fluorine-modified cobalt catalysts for the electrocatalytic hydrogenation of quinoline,[20] and Liu *et al.* systematically reviewed the research progress on nanomaterials for electrocatalytic organic hydrogenation using water as the hydrogen source.[22]

Among the various electrode materials, transition metal oxides are considered promising candidates for use in electrocatalytic hydrogen storage systems because of their rich valence states, low activation energy for electron transport, low cost, nontoxicity, high stability, and good conductivity.[25] Spinel-type $CuCo_2O_4$ offers advantages such as superior performance compared with single cobalt or copper oxides and tunable electronic/structural properties, making it a potential transition metal catalyst for organic hydrogenation. In recent years, researchers have adopted heterostructure construction strategies to enhance their performance. For example, Wang *et al.* reported the use of $CuCo_2O_4$/NF for the electrocatalytic hydrogenation of quinoxaline;[26] Liu *et al.* reported a plasma-induced oxygen vacancy $CuCo_2O_4$/CuO heterostructure for nitrate electroreduction.[27] However, its slow ion diffusion rate and low electronic conductivity limit its catalytic activity. In recent years, a built-in electric field (BIEF) has proven to be an effective strategy for modulating the catalytic electronic structure and optimizing reaction pathways.[28] For example, Tian *et al.* reported the mechanism of BIEF-enhanced hydrogen evolution from ammonia borane hydrolysis in $CuCo_2O_4$–CuO heterostructures;[28] Liu *et al.* studied Mo-doped Cu/Co oxide heterostructures for the HER.[29]

Consequently, researchers have developed various strategies, including cation doping, anion doping, heterointerface construction, and defect engineering.[30–33] For instance, the synergistic effect of Ni^{2+} ions with SnS has been demonstrated to significantly enhance the electrochemical performance of all-solid-state symmetric supercapacitors, underscoring the critical role of cation modulation in transition-metal chalcogenides for energy storage applications.[34] Among these, constructing heterointerfaces is an effective approach to enhance charge transfer and improve conductivity. The effectiveness stems from the differences in work function and energy levels between dissimilar semiconductors. The p–n, p–p, or n–n junctions formed at the interface provide a strong driving force for charge transfer.[35]

Many metal oxides, such as MoO_3, WO_3 and V_2O_5, can exist as layered crystals. Two-dimensional (2D) nanosheets exhibit stable physicochemical properties.[36] Among them, MoO_3 is considered an ideal charge storage platform because of its fast intercalation pseudocapacitance, high theoretical specific capacitance, and wide potential window.[37] Similarly, MXene-based materials, such as $Ti_3C_2T_x$ nanosheets, have been explored for use in the electrocatalytic HER and have demonstrated promising activity and stability in alkaline media.[38] Furthermore, with its 2D/three-dimensional (3D) multiscale structure and synergistic coupling with metals, MoO_3 holds promise for replacing precious metals with low-cost alternatives to achieve superior electrocatalytic activity.[39] In the field of electrocatalysis, MoO_3 has been used to construct high-performance heterojunction catalysts. For example, Hou *et al.* reported that the use of a MoO_3/CoP/rGO heterojunction optimizes the hydrogen evolution reaction (HER) performance through electron redistribution.[40] For instance, a self-supported heterostructure electrocatalyst, namely, MoO_3/NiFe-NF, was constructed *via* hydrothermal and electrodeposition methods and demonstrated excellent performance for both the oxygen evolution reaction (OER) and the HER.[41] An ultralow voltage of 1.43 V was required to achieve a current density of 10 mA cm^{-2} for overall water splitting, surpassing that of commercial precious metal catalysts. Zhang *et al.* systematically summarized the application of heterointerface engineering in overall water splitting.[32] In a parallel strategy, Diyali *et al.* recently reported an operando electro-oxidation reconstitution of a newly designed 2D Co(II)-MOF (NBU-4) on nickel foam into cobalt oxyhydroxide nanosheets. The resulting bifunctional catalyst delivered low overpotentials of 76 mV (HER) and 336 mV (OER) at 10 mA cm^{-2}, a cell voltage of 1.65 V for overall water splitting, and excellent stability over 50 h.[42] In another study, branched MoS_2/MoO_3 heteronanosheets were synthesized using a one-step hydrothermal method;[43] the introduction of sulfur and oxygen vacancies significantly increased the conductivity and charge migration rate, leading to a remarkable improvement in HER activity.

On the basis of the preceding analyses, this study focused on developing a nonprecious metal electrocatalytic system that efficiently drives the hydrogenation of N-heterocyclic compounds under mild conditions. Unlike conventional pathways, which require high temperatures, high pressures, and precious metals, in this work, we designed and fabricated a self-supported electrode by precisely constructing a $Cu_{0.95}Co_{2.05}O_4/MoO_3$ heterojunction on a 3D NF. The core innovation of this design is its use of the interfacial electron induction effect to create functionally differentiated dual active sites. Electron-rich Cu sites increase substrate adsorption and hydrogenation. Moreover, electron-deficient Mo/Co sites efficiently activate water molecules to generate reactive hydrogen species. Interfacial charge transfer further drives the rapid surface migration of these species. This architecture fundamentally optimizes the reaction pathway and kinetics. Consequently, efficient and highly selective pyrazine ECH can be obtained using water as the hydrogen source under ambient conditions. This research not only

provides new materials and strategies for mild hydrogen storage and the release of N-heterocyclic LOHCs but also offers novel insights for designing high-performance heterojunction electrocatalysts.

2 Experimental section

2.1 Sample preparation

Commercially available NF was cut into pieces measuring 2.0 cm × 3.0 cm × 2.0 mm. These pieces were sequentially ultrasonicated in absolute ethanol and 2.0 M HCl for 5 min each and then rinsed with deionized water and absolute ethanol. They were then dried quickly at room temperature for subsequent use.

In a single-compartment cell with a Pt plate (10 mm × 10 mm) as the counter electrode and a saturated calomel electrode (SCE) as the reference electrode, the as-prepared NF electrode (10 mm × 10 mm × 2 mm) was used as the working electrode, with 50 mL of deionized water containing 1.962 g of $Na_2MoO_4{\cdot}2H_2O$ as the electrolyte. Cyclic voltammetry (CV) scanning was performed for 50 cycles within the potential range of −1.245 V to 0.155 V. After deposition, the MoO_3/NF electrode was vacuum-dried for 12 h. Subsequently, the MoO_3/NF electrode and 50 mL of deionized water containing 0.79 g of $Co(NO_3)_2{\cdot}6H_2O$, 0.30 g of $Cu(NO_3)_2{\cdot}3H_2O$, 0.30 g of NH_4F, and 0.60 g of urea were transferred into a 100 mL Teflon-lined stainless-steel autoclave and maintained at 120 °C for 6 h. After natural cooling to room temperature, the product was alternately rinsed with deionized water and ethanol, then vacuum-dried at 60 °C for 8 h and finally calcined in air at 400 °C for 3 h to yield the $Cu_{0.95}Co_{2.05}O_4/MoO_3$/NF catalyst.

For comparison, $Cu_{0.95}Co_{2.05}O_4$/NF was prepared on bare NF using the same hydrothermal procedure, omitting only the MoO_3 electrodeposition step.

2.2 Material characterization

The surface shapes and structures were observed using a Hitachi SU8010 scanning electron microscope (SEM) with a detector at an acceleration voltage of 10 kV. SEM was also used to compare the morphological changes before and after cycling tests to assess stability. An attached Bruker XFlash 610-H energy-dispersive spectrometer (EDS) was used to analyze the semiquantitative composition and elements on the catalyst surface. Transmission electron microscopy (TEM) was performed using a Thermo Fisher-Talos F200X electron microscope with selected area electron diffraction (SAED) and fast Fourier transform (FFT) patterns. The size and chemical composition of the material were analyzed by high-resolution TEM (HRTEM) equipped with a field emission gun on copper mesh. X-ray photoelectron spectroscopy (XPS) measurements were performed on a Thermo Scientific Escalab spectrometer with a monochromatic Al Kα (1486.6 eV) source and a concentric hemispherical energy analyzer to analyze the chemical composition and metal valence states. The changes in the valence states before and after the catalytic reaction were investigated.

The products of the ECH reaction were qualitatively and quantitatively analyzed using Agilent 8860-5977B gas chromatography (GC). The GC system was equipped with an AB-1 capillary column (30 m × 0.250 mm) with a film thickness of 0.25 μm. The injection port temperature was set at 280 °C, and the oven temperature was maintained at 300 °C. The temperature program involved heating from 70 to 180 °C at a ramp rate of 10 °C min^{-1}.

2.3 Electrochemical measurements

2.3.1 Electrochemical systems. Electrochemical tests were performed using a CHI660D electrochemical workstation with a typical three-electrode setup in the H-type cell. Prior to formal testing, each electrochemical system underwent an activation process *via* potentiostatic or galvanostatic conditioning until a stable current–time (*i*–*t*) response was attained.

In an H-type cell separated by a glass frit, a Pt plate (10 mm × 10 mm) was used as the counter electrode, a Hg/HgO electrode was used as the reference electrode, and a catalyst electrode (10 mm × 10 mm × 2 mm) was used as the working electrode.

The working electrode compartment contained 40 mL of 1 M KOH or 1 M KOH + 10 mM pyrazine, while the counter electrode compartment contained 40 mL of 1 M KOH (pH 13.8).

All the electrochemical tests were performed at 25 °C and atmospheric pressure. All recorded potentials were calibrated to the reversible hydrogen electrode (RHE) with eqn (1).

$$E_{RHE}\,(V) = E_{(Hg/HgO)} + 0.0591 \times pH + E^{0}_{(Hg/HgO)} + 0.059 \times pH + 0.098 \quad (1)$$

2.3.2 Linear sweep voltammetry. Linear sweep voltammetry (LSV) measurements were performed with and without 10 mM pyrazine. The electrocatalysts served as the working electrodes. The LSV scans were conducted at 5 mV s^{-1} under stirring over a potential range of −0.45 to −0.60 V (*vs.* RHE).

2.3.3 Tafel analysis. The Tafel slopes were derived by fitting selected data from the LSV measurements using eqn (2):

$$\eta = a + b \times \log j \quad (2)$$

where η is the overpotential (V), a is a constant, b is the Tafel slope (mV dec^{-1}), and j is the current density (mA cm^{-2}).

2.3.4 Cyclic voltammetry. Cyclic voltammetry (CV) tests were carried out in 40 mL of 1 M KOH in the cathodic compartment, with and without 10 mM pyrazine. The four catalysts were used as working electrodes to compare their catalytic performance. The CV measurements were performed at a scan rate of 5 mV s^{-1} under stirring between −0.3 and −0.7 V (*vs.* RHE).

2.3.5 Electrochemical impedance spectroscopy. Electrochemical impedance spectroscopy (EIS) was employed to investigate the charge-transfer kinetics of the catalysts. The measurements were conducted at a fixed potential of −0.25 V (*vs.* RHE) with a 5 mV AC amplitude over a frequency range from 10 kHz to 0.01 Hz. The obtained EIS data were fitted using an equivalent circuit model *via* Zview software to extract relevant electrochemical parameters.

2.3.6 Double-layer capacitance and electrochemically active surface area. CV was performed within a non-Faradaic potential window of ±50 mV around the open-circuit potential at various scan rates (20, 40, 60, 80, and 100 mV s^{-1}). The double-layer capacitance (C_{dl}) was determined from the slope of the charge current *versus* scan rate plot. The electrochemically active surface area (ECSA) was then estimated with eqn (3).

$$\mathrm{ECSA} = C_{dl}/C_s \quad (3)$$

where C_s, the specific capacitance for a flat surface, was taken as 0.04 mF cm^{-2} in KOH solution.[44]

2.3.7 Chronoamperometry. The reaction was conducted at a constant potential of −0.25 V (*vs.* RHE) for 1.5 h, after which the pyrazine conversion and product selectivity were quantified by GC. The pyrazine conversion and the piperazine selectivity of ECH were calculated with eqn (4) and (5).

$$\text{Conversion}\ (\%) = \frac{M_1}{M_2} \times 100\% \quad (4)$$

where M_1 represents the amount of substrate consumed (mol), and M_2 represents the initial amount of substrate (mol).

$$\text{Selectivity}\ (\%) = \frac{M_3}{M_1} \times 100\% \quad (5)$$

Here, M_3 denotes the amount of target product formed (mol).

3 Results and discussion

3.1 Physical characterization

3.1.1 SEM and EDS. MoO_3 spreads over the surface of the NF in a layered, two-dimensional manner, forming a smooth and uniform covering layer (Fig. 1a–c). $Cu_{0.95}Co_{2.05}O_4$/NF grows *in situ* on the NF (Fig. 1d–f), forming nanoflake aggregates with flower-like or spherical morphologies. These nanoflakes self-assemble into spherical or quasispherical microstructures through layer-by-layer folding and curling. Their surfaces have dense wrinkles, which significantly increases the electrochemically active surface area and exposes many active sites, thus facilitating the adsorption of the reactive hydrogen intermediate (H*). Upon incorporation of MoO_3, the $Cu_{0.95}Co_{2.05}O_4/MoO_3$ composite underwent distinct morphological evolution (Fig. 1g–i). Finer needle-like protrusions emerge on the nanoflake surfaces, forming an interconnected 3D porous network. This architecture significantly increases the active surface area and the number of catalytic active sites, thus increasing the C_{dl} and ECSA for superior catalytic performance. Furthermore, the abundant pore structure provides shortened diffusion pathways and a highly accessible transport network for both electrolyte ions and pyrazine molecules, which substantially improves mass transport and reaction kinetics. The robust integration of this 3D framework with the NF substrate ensures sustained high catalytic efficiency and conversion rates even under high current densities of the LSV results and contributes to remarkable structural integrity during prolonged cycling. This is consistent with the excellent stability observed in subsequent tests. The EDS mappings confirm the homogeneous distribution of all the constituent elements in MoO_3/NF (Fig. 1b$_{1-3}$), $Cu_{0.95}Co_{2.05}O_4$/NF (Fig. 1e$_{1-4}$), and $Cu_{0.95}Co_{2.05}O_4/MoO_3$/NF (Fig. 1h$_{1-5}$), with no detectable impurity elements, successfully verifying the synthesis of the target materials.

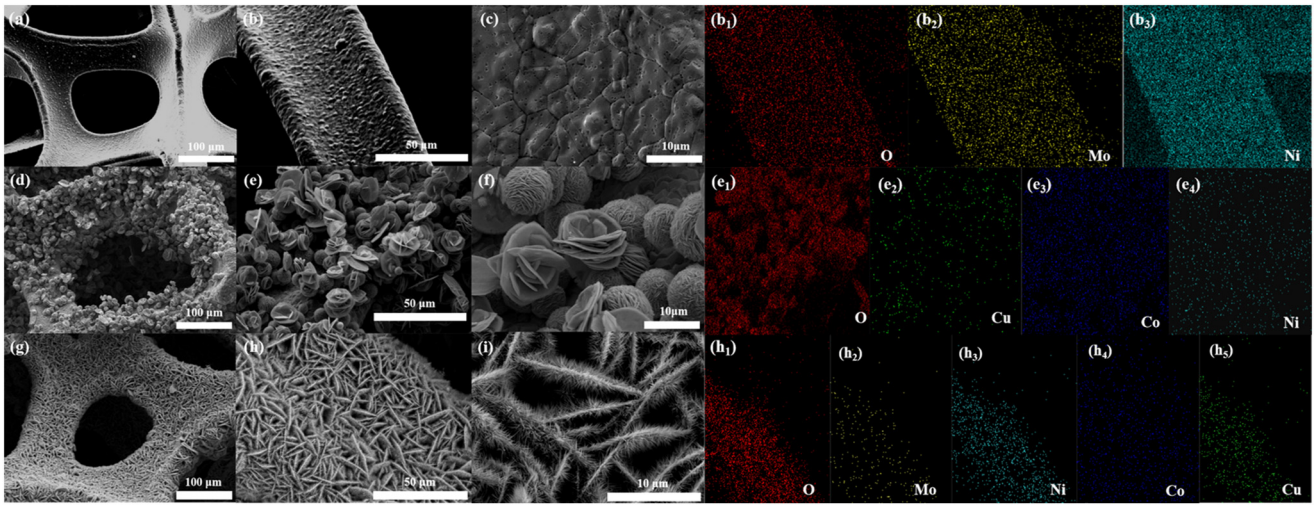

Fig. 1 SEM images and corresponding EDS elemental mapping of (a–c and b$_{1-3}$) MoO_3/NF, (d–f and e$_{1-4}$) $Cu_{0.95}Co_{2.05}O_4$/NF, and (g–i and h$_{1-5}$) $Cu_{0.95}Co_{2.05}O_4/MoO_3$/NFs.

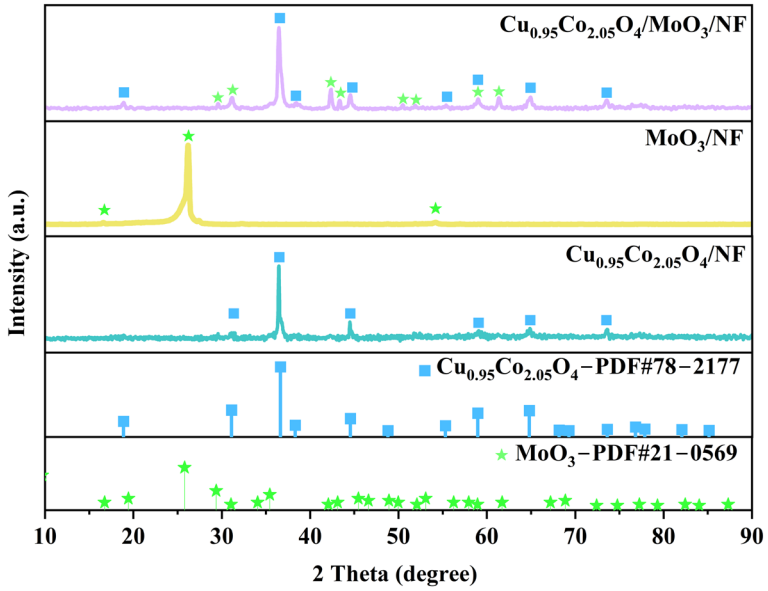

Fig. 2 XRD patterns of the catalysts.

3.1.2 XRD. The characteristic diffraction peaks at 18.88°, 31.08°, 36.62°, 38.31°, 44.53°, 55.29°, 58.96°, 64.79°, and 73.60° of $Cu_{0.95}Co_{2.05}O_4/MoO_3$/NF are assigned to the (111), (220), (311), (222), (400), (422), (511), (440), and (620) crystal planes of the spinel $Cu_{0.95}Co_{2.05}O_4$ phase (PDF#78-2177), respectively (Fig. 2). Furthermore, the peaks at 29.36°, 31.03°, 42.05°, 43.10°, 49.96°, 52.07°, 58.93°, and 63.71° of $Cu_{0.95}Co_{2.05}O_4/MoO_3$/NF match well with the characteristics of the (300), (204), (224), (320), (500), (330), (424), and (430) reflections of MoO_3 (PDF#21-0569), respectively. The characteristic diffraction peaks at 31.08°, 36.62°, 44.53°, 58.96°, 64.79°, and 73.60° of $Cu_{0.95}Co_{2.05}O_4$/NF are assigned to the (220), (311), (400), (511), (440), and (620) crystal planes of the spinel $Cu_{0.95}Co_{2.05}O_4$ phase (PDF#78-2177), respectively. Similarly, the peaks at 16.75°, 25.80°, and 53.08° for MoO_3/NF correspond well to the (110), (210), and (420) planes of MoO_3 (PDF#21-0569), respectively. These results confirm the successful preparation of the target catalysts. For the $Cu_{0.95}Co_{2.05}O_4/MoO_3$/NF composite, the XRD patterns clearly demonstrate the successful integration of the spinel $Cu_{0.95}Co_{2.05}O_4$ phase with MoO_3. This composite is not a simple physical mixture. Instead, it establishes the foundation for forming a BIEF at the heterojunction interface between $Cu_{0.95}Co_{2.05}O_4$ and MoO_3. The difference in the work function between the two phases induces spontaneous charge transfer across the interface. This directly affects the electron density of the interfacial metal active sites, consequently influencing their adsorption and activation behaviors toward the reactants (H_2O and pyrazine). Such interfacial engineering enables the optimization of reactant adsorption strength and reaction pathways at distinct sites. This represents the key structural design for achieving synergistic enhancement of both high activity and high selectivity. The specific changes in the electronic structure resulting from this interfacial effect are directly evidenced by the results of the subsequent XPS analysis.

The low-magnification TEM image shows that the material is uniformly dispersed without significant agglomeration, with particle sizes of approximately 10–20 nm (Fig. 3a). The overall structure exhibits a worm-like porous morphology, primarily assembled from $Cu_{0.95}Co_{2.05}O_4$ nanoparticles, within which MoO_3 exists in an amorphous state. The HRTEM image reveals interplanar spacings of 0.246 and 0.156 nm, corresponding to the (311) plane of $Cu_{0.95}Co_{2.05}O_4$ and the (430) plane of MoO_3, respectively (Fig. 3b). A clear heterojunction interface between the two phases is observed. This intimate interfacial contact is the physical prerequisite for efficient charge transfer and H* spillover. This is crucial for achieving rapid synergy between Co/Mo sites (for H* generation) and Cu sites (for pyrazine adsorption and hydrogenation). The crystallographic structures were further confirmed by the SAED and FFT patterns (Fig. 3c and d), both verifying the coexistence of the crystalline $Cu_{0.95}Co_{2.05}O_4$ and MoO_3 phases. These results confirm the formation of abundant, closely contacted heterojunction interfaces. This ensures that the electron transfer phenomena subsequently observed by XPS originate from real and effective interfacial interactions rather than from surface effects of the isolated phases.

3.1.3 XPS. To explore the interfacial electronic interactions within the $Cu_{0.95}Co_{2.05}O_4/MoO_3$/NF heterojunction, we investigated the valence states and electron redistribution using XPS. The survey spectra confirm the elemental composition (Fig. S1). MoO_3/NF exhibits peaks only for Mo 3d, O 1s, and C 1s, whereas $Cu_{0.95}Co_{2.05}O_4$/NF shows peaks

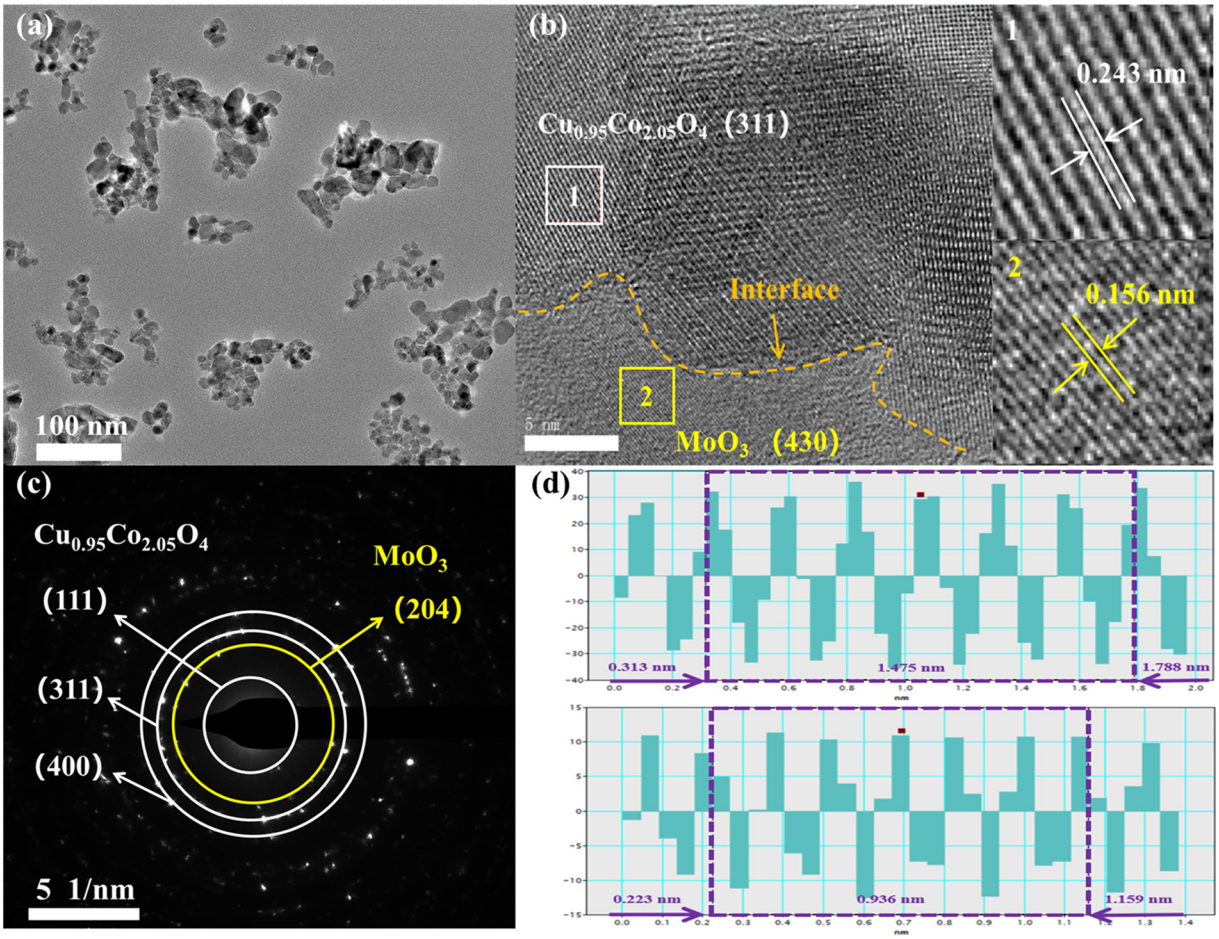

Fig. 3 (a) TEM and (b) HRTEM images and (c) SAED and (d) FFT patterns of $Cu_{0.95}Co_{2.05}O_4/MoO_3$/NF.

for Cu 2p, Co 2p, O 1s, and C 1s. In contrast, $Cu_{0.95}Co_{2.05}O_4/MoO_3$/NF displays distinct peaks for Cu 2p, Co 2p, Mo 3d, O 1s, and C 1s, with no detectable peaks from impurities, which is consistent with the EDS elemental mapping results (Fig. $1b_{1-3}$, e_{1-4} and h_{1-5}). XPS analysis provides insights into the chemical states and electron transfer. In the Cu 2p spectra (Fig. 4a), the peaks for both $Cu_{0.95}Co_{2.05}O_4/MoO_3$/NF and $Cu_{0.95}Co_{2.05}O_4$/NF are assigned to Cu^+, Cu^{2+}, and their satellite peaks.[45] For the composite, the Cu 2p peaks show a negative binding energy shift compared with those of $Cu_{0.95}Co_{2.05}O_4$/NF. Furthermore, the Cu^+/Cu^{2+} peak area ratio increases from 0.21 to 0.34. These changes indicate an increased electron density around Cu atoms at the heterojunction interface, confirming electron transfer from MoO_3 to $Cu_{0.95}Co_{2.05}O_4$. The Co 2p spectra are fitted with contributions from Co^{2+}, Co^{3+}, and satellites (Fig. 4b).[46] A notable change is observed in the Co^{2+}/Co^{3+} peak area ratio. This ratio increases dramatically from 0.33 in pure $Cu_{0.95}Co_{2.05}O_4$/NF to 3.54 in the $Cu_{0.95}Co_{2.05}O_4/MoO_3$/NF heterostructure. The increased Co^{2+} content suggests that $Cu_{0.95}Co_{2.05}O_4$ in the composite accepts electrons, leading to the reduction of higher-valent Co ions. The O 1s spectra of all three catalysts can be deconvoluted into three contributions: lattice oxygen (O_L), oxygen vacancies (O_V), and adsorbed water/carbonate species (O_C) (Fig. 4c).[47] Notably, the O 1s binding energies remain almost unchanged across the samples. This suggests that O atoms are not directly involved in interfacial electron transfer within the heterojunction.

For Mo 3d, the spectrum of $Cu_{0.95}Co_{2.05}O_4/MoO_3$/NF shows a doublet at 232.13 eV (Mo $3d_{5/2}$) and 235.28 eV (Mo $3d_{3/2}$), characteristic of Mo^{6+} (Fig. 4d).[48] Compared with those of pure MoO_3/NF, these peaks exhibit a positive binding energy shift, indicating a decreased electron density around the Mo atoms at the interface. In summary, charge transfer between the two components at the $Cu_{0.95}Co_{2.05}O_4/MoO_3$/NF heterointerface promotes interfacial charge reorganization. This results in an electron-rich state for $Cu_{0.95}Co_{2.05}O_4$ and an electron-deficient state for MoO_3 at the interface. The observed binding energy shifts and changes in the valence state ratios provide clear evidence for the directional electron transfer from MoO_3 to $Cu_{0.95}Co_{2.05}O_4$. This process establishes a BIEF directed from MoO_3 toward $Cu_{0.95}Co_{2.05}O_4$ across the interface. This BIEF modulates the catalytic behavior by inducing functional differentiation of the active sites through the tailoring of the electronic structure. The electron-rich region enhances pyrazine adsorption and hydrogenation, whereas the electron-deficient region

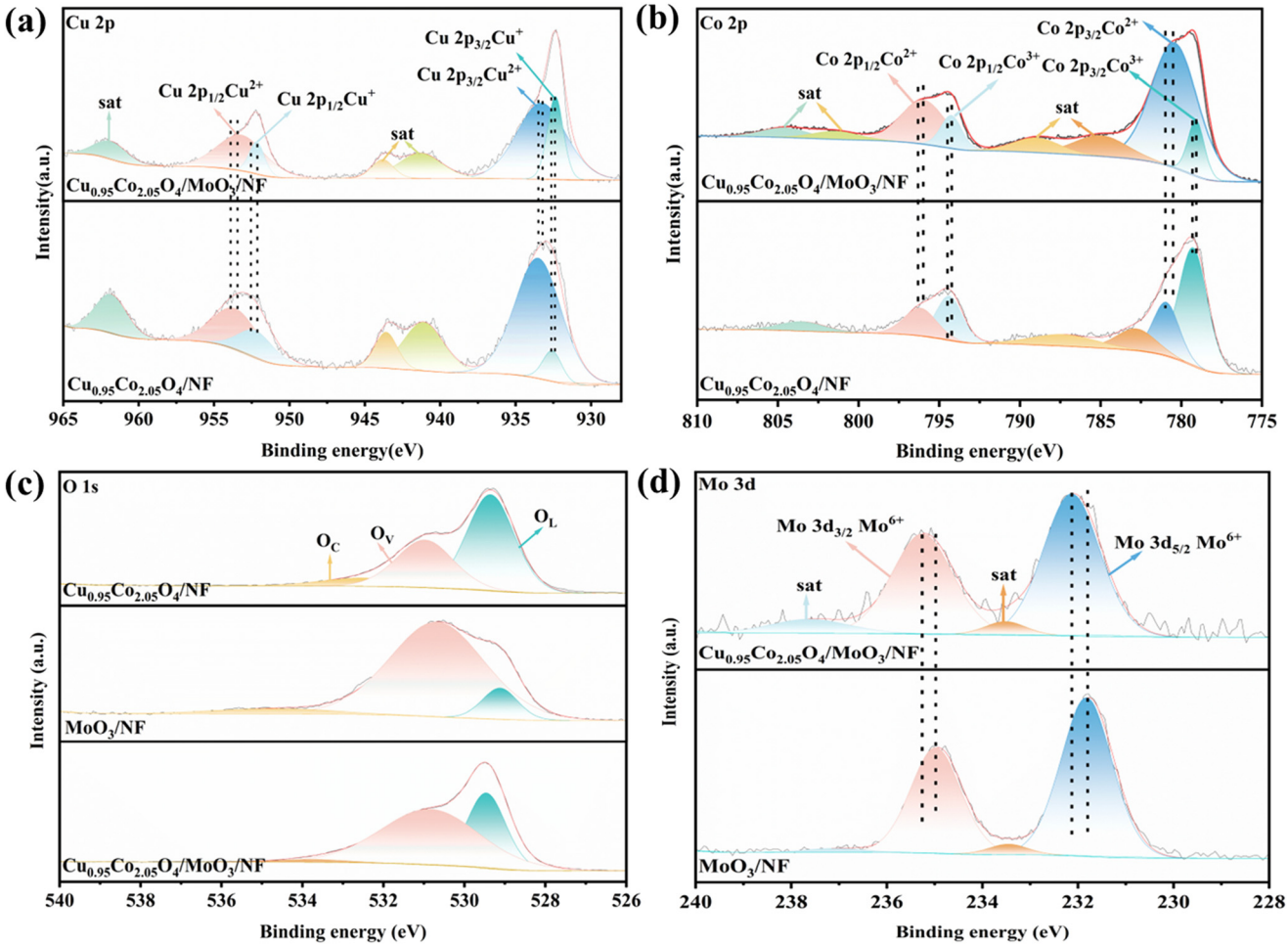

Fig. 4 (a) Cu 2p, (b) Co 2p, (c) O 1s and (d) Mo 3d XPS spectra of the catalysts.

promotes water dissociation and H* generation. Simultaneously, it drives interfacial charge separation, creating a localized "reactor" environment that facilitates the surface spillover of H* species to the adsorption sites for hydrogenation, thus suppressing the competing HER. Furthermore, the Co^{2+} and electron-deficient Mo sites promote the Volmer step, and the Cu^{+} sites optimize the pyrazine adsorption and hydrogenation steps. This synergistic effect leads to faster apparent reaction kinetics. In electrochemical tests, this is evidenced by a lower Tafel slope and a lower charge transfer resistance. Consequently, a high current density and high conversion efficiency are achieved at a relatively low overpotential of −0.25 V (*vs.* RHE).

3.2 Electrochemical analysis

3.2.1 CV. In both electrolytes, NF and MoO_3/NF exhibited negligible redox features and extremely low current densities within the potential window of −0.3 to −0.7 V (*vs.* RHE) (Fig. 5a and b). These findings indicate that NF and MoO_3/NF are essentially inert toward the HER and have weak catalytic activity for pyrazine hydrogenation under alkaline conditions. The CV curves of $Cu_{0.95}Co_{2.05}O_4$/NF in both electrolytes show a pair of redox peaks (Fig. 5c). The reduction and oxidation peaks are at approximately 0.36 and 0.57 V (*vs.* RHE), respectively, in both 1 M KOH and 1 M KOH containing 0.01 M pyrazine. These peaks are attributed to the redox reactions of Cu species. The CV profiles and peak potentials are similar for the two electrolytes. For the $Cu_{0.95}Co_{2.05}O_4/MoO_3$/NF composite, the CV curves in the pyrazine-containing electrolyte show reduction and oxidation peaks at 0.36 and 0.58 V, respectively (Fig. 5d). These values show only minor shifts compared with the peaks at 0.35 and 0.57 V observed in pure 1 M KOH. This demonstrates that the introduction of MoO_3 effectively stabilizes the redox-active centers of $Cu_{0.95}Co_{2.05}O_4$. The redox characteristics remain largely unchanged even in the presence of adsorbing species, suggesting enhanced electrochemical reversibility and structural stability. This stabilization likely stems from the modulating effect of MoO_3 on the active sites and the promoted interfacial charge transfer.

3.2.2 LSV and Tafel slope. In 1.0 M KOH, $Cu_{0.95}Co_{2.05}O_4/MoO_3$/NF exhibited a substantially higher current density than

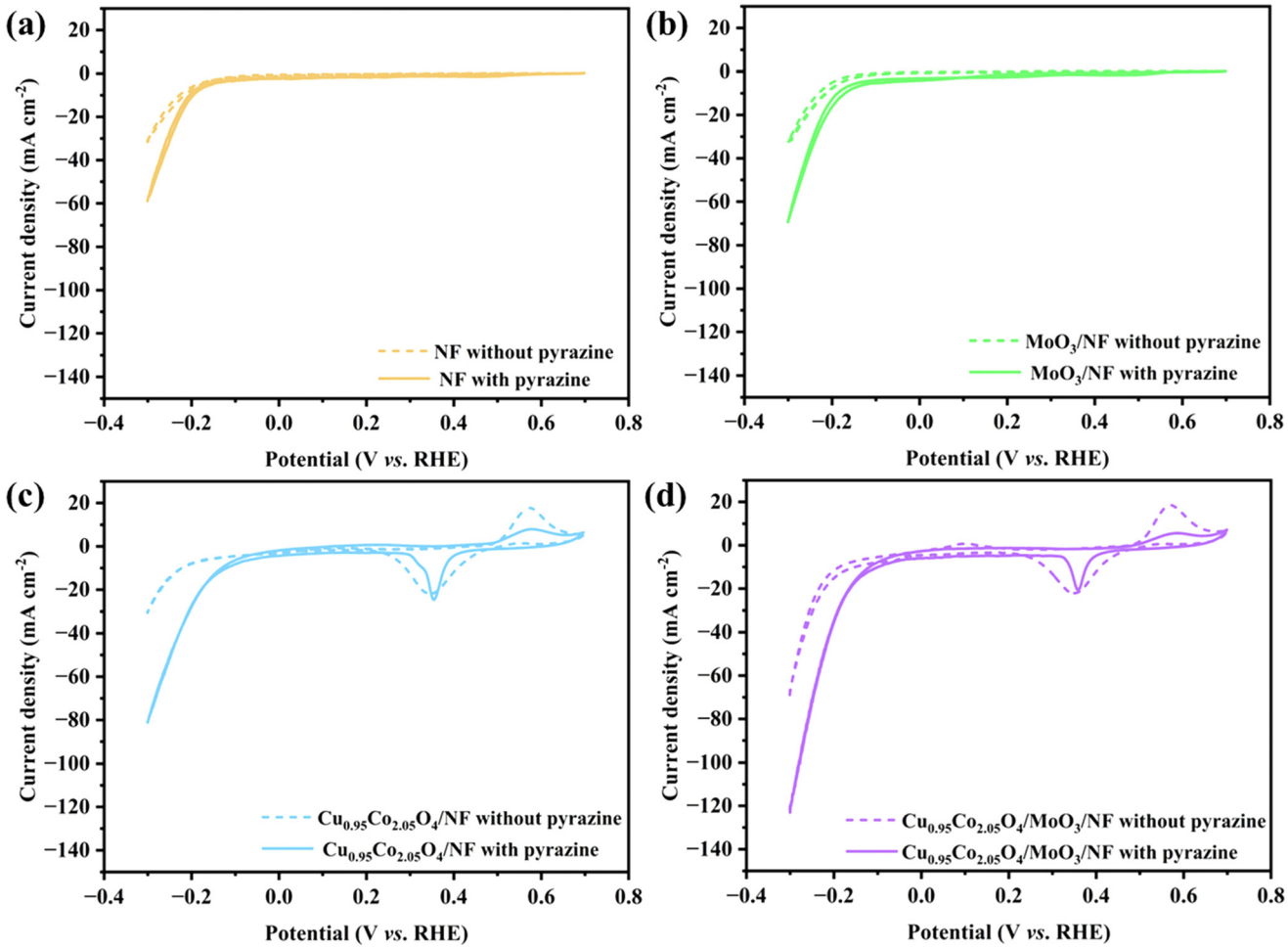

Fig. 5 CV curves at 5 mV s^{-1} from −0.3 to −0.7 V (*vs.* RHE) for the (−) catalyst | 1 M KOH + 10 mM pyrazine (or 1 M KOH) || 1 M KOH | Pt (+) with a Hg/HgO electrode as the reference electrode and (a) NF, (b) MoO_3/NF, (c) $Cu_{0.95}Co_{2.05}O_4$/NF, or (d) $Cu_{0.95}Co_{2.05}O_4$/MoO_3/NF as the working electrode.

$Cu_{0.95}Co_{2.05}O_4$NF and MoO_3/NF did (Fig. 6a), which is consistent with previous reports that three-dimensional self-supported architectures enhance the electrocatalytic performance. Upon the addition of pyrazine, the current increase was most pronounced for $Cu_{0.95}Co_{2.05}O_4$/MoO_3/NF, indicating that the ECH of pyrazine is thermodynamically more favorable than the competing HER. To correlate the Tafel slopes with the reaction mechanism, we analyzed the Tafel slopes of the different catalysts in 1 M KOH containing pyrazine (Fig. 6b and Table S1). The obtained Tafel slopes were 156.22, 195.80, 212.08, and 254.89 mV dec^{-1} for $Cu_{0.95}Co_{2.05}O_4$/MoO_3/NF, $Cu_{0.95}Co_{2.05}O_4$/NF, MoO_3/NF, and bare NF, respectively. All values are higher than the theoretical Tafel slope for the Volmer step in the alkaline HER (≈120 mV dec^{-1}), suggesting that water dissociation to generate active hydrogen (H*) is the rate-determining step. Among the catalysts, the heterojunction composite had the lowest Tafel slope, which was significantly lower than those of the individual components. This finding indicates that the heterojunction effectively reduces the energy barrier of the Volmer step, thus accelerating water activation and H* generation. A lower Tafel slope corresponds to a higher charge-transfer coefficient, confirming that the built-in electric field at the heterointerface promotes electron transfer to water molecules. This trend is consistent with the hydrogenation performance: the catalyst with the lowest Tafel slope simultaneously achieved the highest pyrazine conversion and piperazine selectivity, directly supporting the built-in-electric-field-driven mechanism. In contrast, MoO_3/NF and bare NF had Tafel slopes above 200 mV dec^{-1}, indicating weak water activation capability, sluggish H* generation, and a lack of effective hydrogenation sites; their current response was dominated by the HER. $Cu_{0.95}Co_{2.05}O_4$/NF showed some activity, but without the electronic modulation provided by MoO_3, its water activation kinetics remained insufficient.

3.2.3 C_{dl} and EIS. The ECSA of the catalysts was quantitatively assessed *via* C_{dl} measurements in the non-Faradaic potential region, with CV curves recorded at various scan rates (Fig. S2). The fitted C_{dl} values of $Cu_{0.95}Co_{2.05}O_4$/MoO_3/NF, $Cu_{0.95}Co_{2.05}O_4$/NF, MoO_3/NF and bare NF were 15.66, 11.30, 0.91 and 0.67 mF

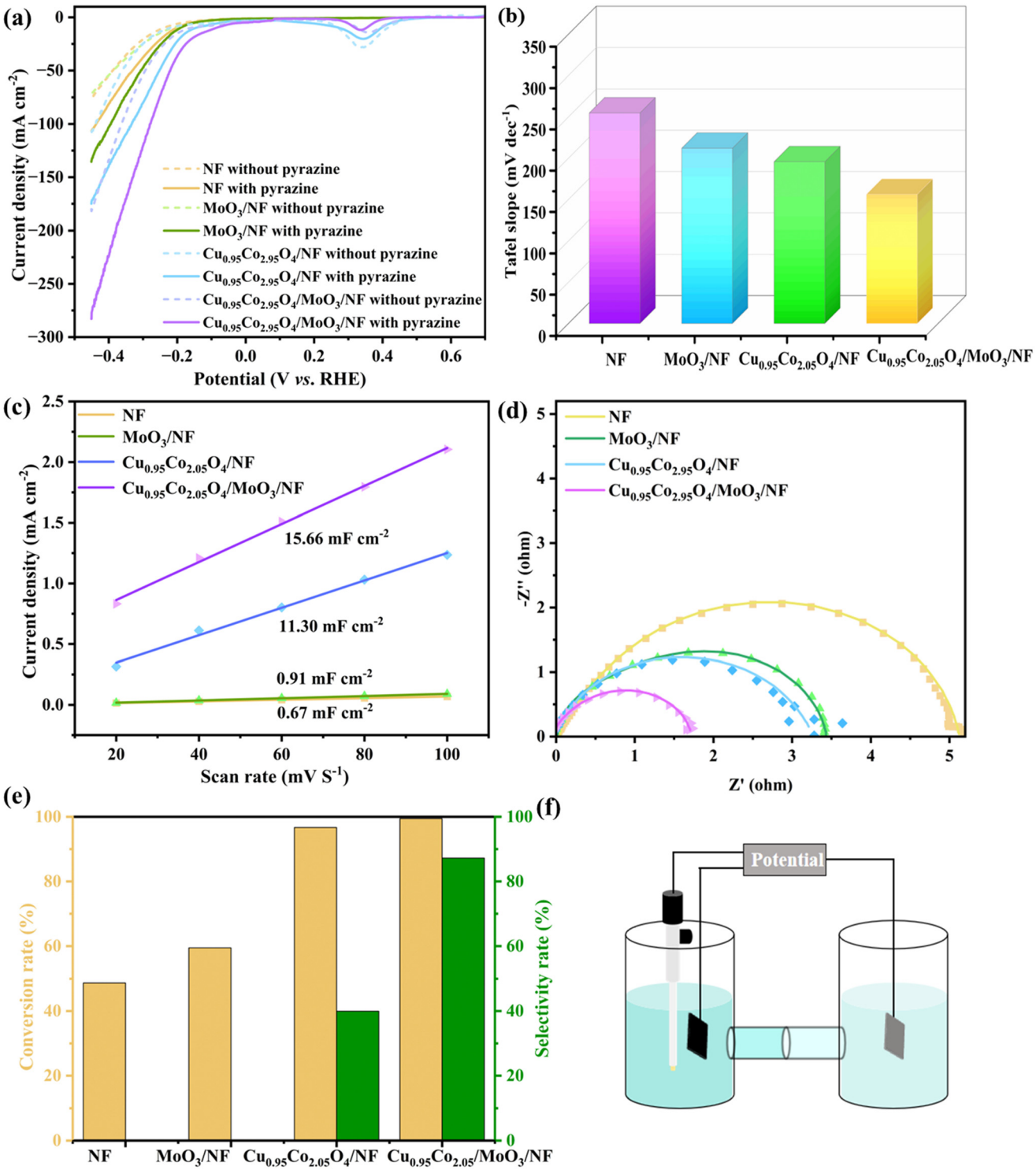

Fig. 6 (a) LSV curves, (b) Tafel plots, (c) C_{dl}, (d) Nyquist plots, (e) pyrazine conversion and piperazine selectivity after chronoamperometry at −0.25 V (*vs.* RHE) for 1.5 h, and (f) schematic of the reaction setup for the catalysts.

cm^{-2}, respectively (Fig. 6c and Table S1). The higher C_{dl} values of the former two catalysts indicate a larger ECSA and more exposed active sites.

To gain deeper insight into the charge transfer process, the electrochemical impedance spectroscopy (EIS) spectra were fitted using an equivalent circuit, where R_s represents the solution resistance and R_{ct} represents the charge transfer resistance. The detailed fitted parameters are summarized in Table S1. The results show that the R_{ct} value of $Cu_{0.95}Co_{2.05}O_4/MoO_3/NF$ (0.84 Ω) is considerably lower than those of $Cu_{0.95}Co_{2.05}O_4/NF$ (1.69 Ω) and MoO_3/NF (1.71 Ω). This finding indicates that the construction of the

heterointerface significantly reduces the energy barrier for the electrochemical reaction and accelerates interfacial electron transfer. These findings are consistent with the three-dimensional burr-like nanosheet structure observed by SEM, which facilitates the exposure of more active sites and promotes mass transport. The low R_{ct}, together with the high ECSA, synergistically accounts for the excellent performance of this catalyst in the electrocatalytic hydrogenation of pyrazine.

Pyrazine hydrogenation tests after chronoamperometry at −0.25 V (*vs.* RHE) for 1.5 h revealed that $Cu_{0.95}Co_{2.05}O_4/MoO_3$/NF achieved both the highest pyrazine conversion and the highest piperazine selectivity (Fig. 6e and f and S4 and Table S1). This further demonstrates its superior catalytic performance.

3.2.4 Practical scalability. As shown in Fig. S5, after the as-prepared large-scale electrode was cut into a 1.0 cm × 1.0 cm catalyst, its polarization curve was nearly identical to that of the standard-sized electrode. This negligible difference indicates that the electrochemical performance of the catalyst is not limited by mass transport or an ohmic drop associated with electrode scaling under the testing conditions. More importantly, these results highlight the excellent uniformity and reproducibility of the self-supported heterojunction structure on nickel foam, paving the way for potential large-scale application of the catalyst without sacrificing its activity.

3.3 Hydrogenation mechanism of pyrazine

3.3.1 Pyrazine concentration-dependent experiments. To investigate the dependence of the ECH rate on the pyrazine concentration, experiments were performed with varying pyrazine concentrations. The results show that the current density increased significantly when the pyrazine concentration was increased from 5 to 10 mM. These findings indicate that at 5 mM, pyrazine adsorption had not reached saturation on the catalyst surface and that the reaction rate was limited by the pyrazine concentration. However, a further increase in the pyrazine concentration (from 10 to 40 mM) led to a gradual decrease in the current density observed for the $Cu_{0.95}Co_{2.05}O_4/MoO_3$/NF catalyst (Fig. 7a). This phenomenon suggests a competitive adsorption relationship between pyrazine and H* adsorbed on the catalyst surface at high concentrations. The increased pyrazine concentration reduces the surface coverage of H, thus inhibiting the subsequent hydrogenation step and causing an overall decrease in the ECH rate. These findings support a refinement of the pyrazine hydrogenation mechanism from an initial proton-coupled electron transfer (PCET) pathway to a hydrogen atom transfer (HAT) mechanism. In this refined mechanism, H* is first generated *via* electrochemical reduction, followed by a surface reaction with adsorbed pyrazine (the Langmuir–Hinshelwood mechanism). Therefore, the generation and surface coverage of H* play crucial roles in the pyrazine reduction process, and variations in its concentration directly affect the reaction rate.

3.3.2 Investigation of the H* source. The role of H* was probed using *tert*-butanol as a quenching agent. The presence of *tert*-butanol significantly suppressed pyrazine

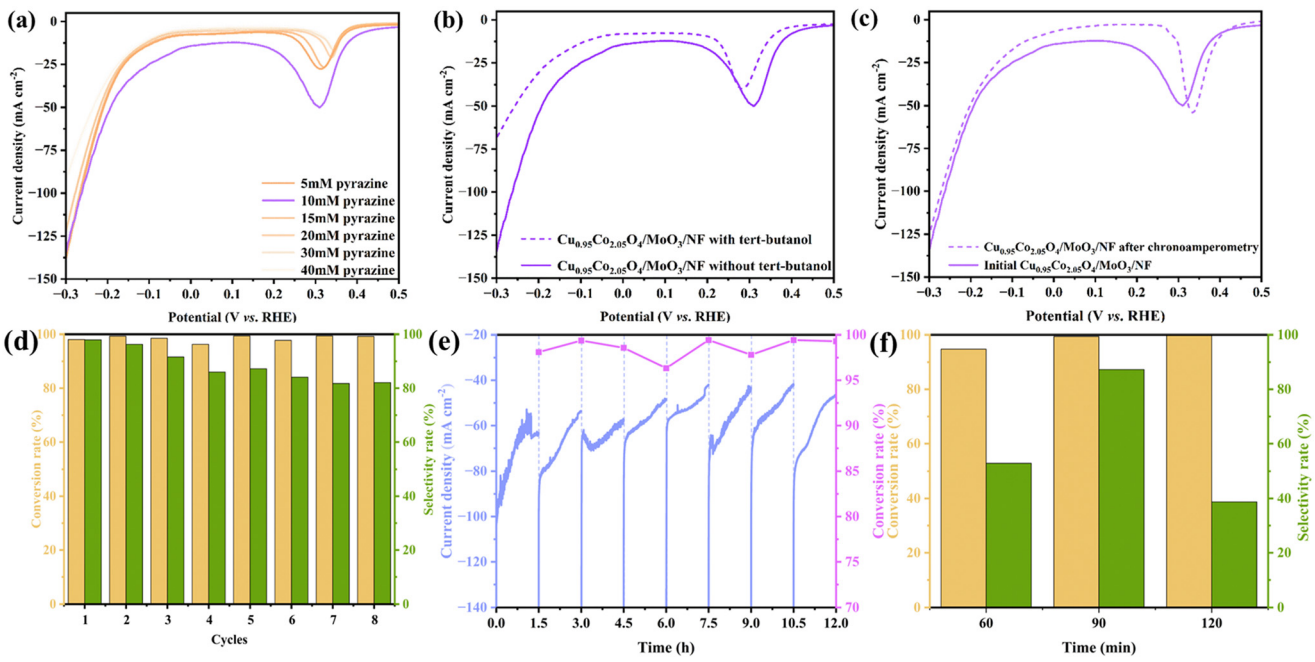

Fig. 7 Electrochemical measurements of $Cu_{0.95}Co_{2.05}O_4/MoO_3$/NF in (−) $Cu_{0.95}Co_{2.05}O_4/MoO_3$/NF (pyrazine/piperazine) | 1 M KOH + 10 mM pyrazine with/without 0.5 mL *tert*-butanol || 1 M KOH + H_2O | Pt (+) (OH^-/O_2). (a) Substrate concentration-dependent tests, (b) LSV curves with and without *tert*-butanol in the potential range of −0.3 to 0.5 V (*vs.* RHE), (c) LSV curves before and after 8 cycles, (d) conversion and selectivity rate under chronoamperometry at −0.25 V (*vs.* RHE) for 1.5 h, (e) current and conversion at different time intervals under chronoamperometry at −0.25 V (*vs.* RHE) for 1.5 h, and (f) time-dependent conversion and selectivity at −0.25 V (*vs.* RHE).

hydrogenation (Fig. 7b). This confirms that H* generated *via* the Volmer step is the key species governing the reaction process.

3.3.3 Identification of active metal sites. To identify the true active sites and evaluate the practical scalability of the $Cu_{0.95}Co_{2.05}O_4/MoO_3$/NF heterojunction, a strong metal-chelating agent, ethylenediaminetetraacetic acid (EDTA), was introduced. As shown in Fig. S6, compared with the EDTA-free condition, the addition of EDTA significantly reduced the current density over the entire potential range. This substantial decrease confirms that the Cu and Co species are the genuine active centers for the electrocatalytic hydrogenation of pyrazine because EDTA preferentially coordinates with the surface metal sites, blocking their accessibility and suppressing hydrogenation activity.

3.3.4 Stability tests. Catalyst stability is a critical performance parameter. The stability of the $Cu_{0.95}Co_{2.05}O_4/MoO_3$/NF system was evaluated by chronoamperometry. The catalyst underwent 8 cycles of chronoamperometry at −0.25 V (*vs.* RHE) for 1.5 h (total of 12 h). The current density remained nearly unchanged after these cycles. Throughout the eight cycles, pyrazine conversion consistently exceeded 95%, and the piperazine selectivity remained above 80%, while the current density was largely stable (Fig. 7d and e). The reaction time for pyrazine ECH over $Cu_{0.95}Co_{2.05}O_4/MoO_3$/NF was optimized. The conversion increased with time, and the selectivity reached its maximum at 90 min (Fig. 7f). In terms of energy efficiency, 90 min was identified as the optimal reaction time for pyrazine ECH.

The SEM image of $Cu_{0.95}Co_{2.05}O_4/MoO_3$/NF after 8 cycles still shows a microstructure composed of irregular nanosheets with burr-like features, accompanied by minor catalyst detachment (Fig. 8a–c). EDS analysis of $Cu_{0.95}Co_{2.05}O_4$/NF after cycling indicated a homogeneous distribution of all the elements (Fig. 8d). After 8 cycles, the O 1s spectrum of $Cu_{0.95}Co_{2.05}O_4/MoO_3$/NF remained dominated by O_V, but the O_C content increased significantly (Fig. 9d). This indicates adsorption of OH^- from the solution phase onto the catalyst surface. In the Mo 3d spectrum (Fig. 9a), the binding energy of the Mo^{6+} peak exhibited a negative shift. This provides further evidence of a higher electron density around Mo^{6+}, which facilitates the adsorption and activation of water molecules. The Co 2p spectrum (Fig. 9b) showed peaks at 795.87 and 779.95 eV attributed to Co^{3+} and peaks at 797.70 and 782.55 eV attributed to Co^{2+}. The intensity of the Co^{2+} peaks decreased relative to that of the Co^{3+} peaks. In the Cu 2p spectrum (Fig. 9c), the peaks at 933.19 and 931.95 eV were assigned to Cu^{2+} and Cu^+ in the Cu $2p_{3/2}$ region, respectively. Peaks at

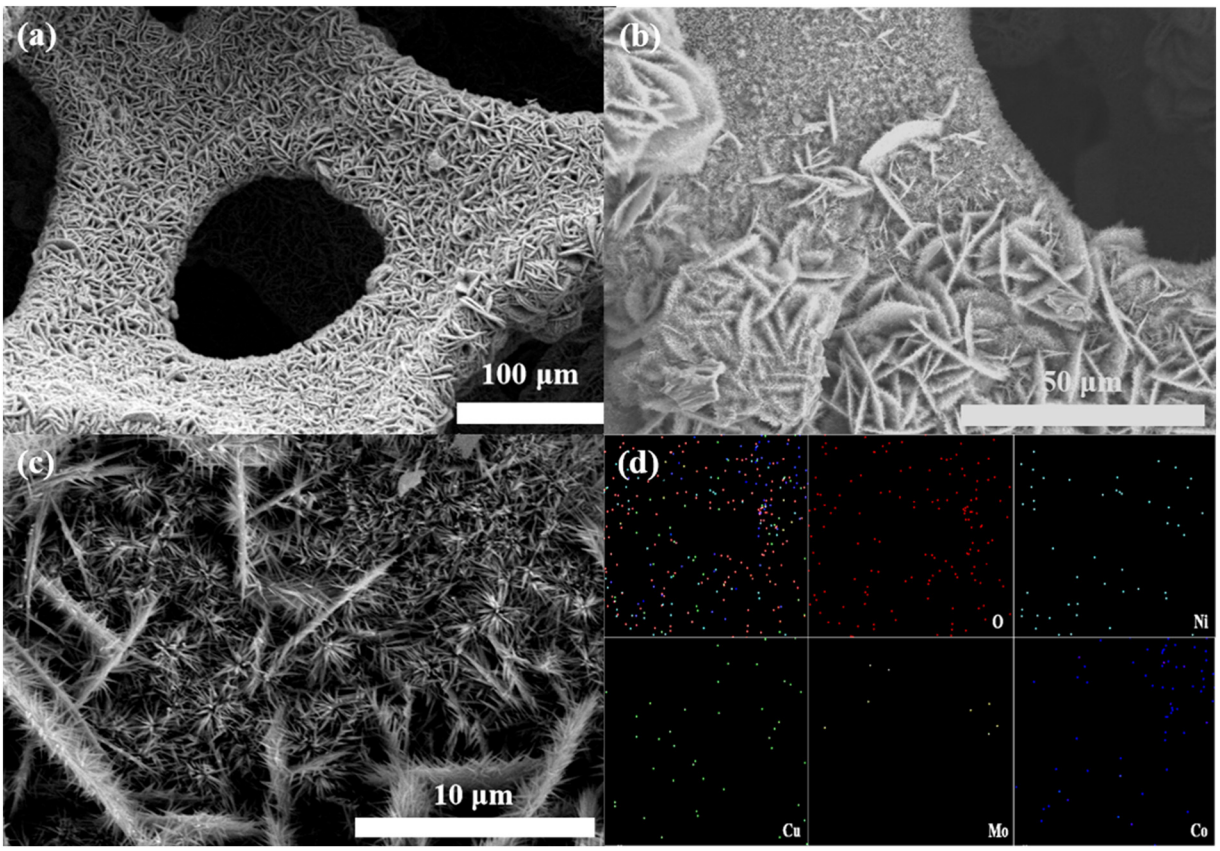

Fig. 8 (a–c) SEM images and (d) EDS mapping of $Cu_{0.95}Co_{2.05}O_4/MoO_3$/NF after 8 cycles of chronoamperometry at −0.25 V (*vs.* RHE) for 1.5 h.

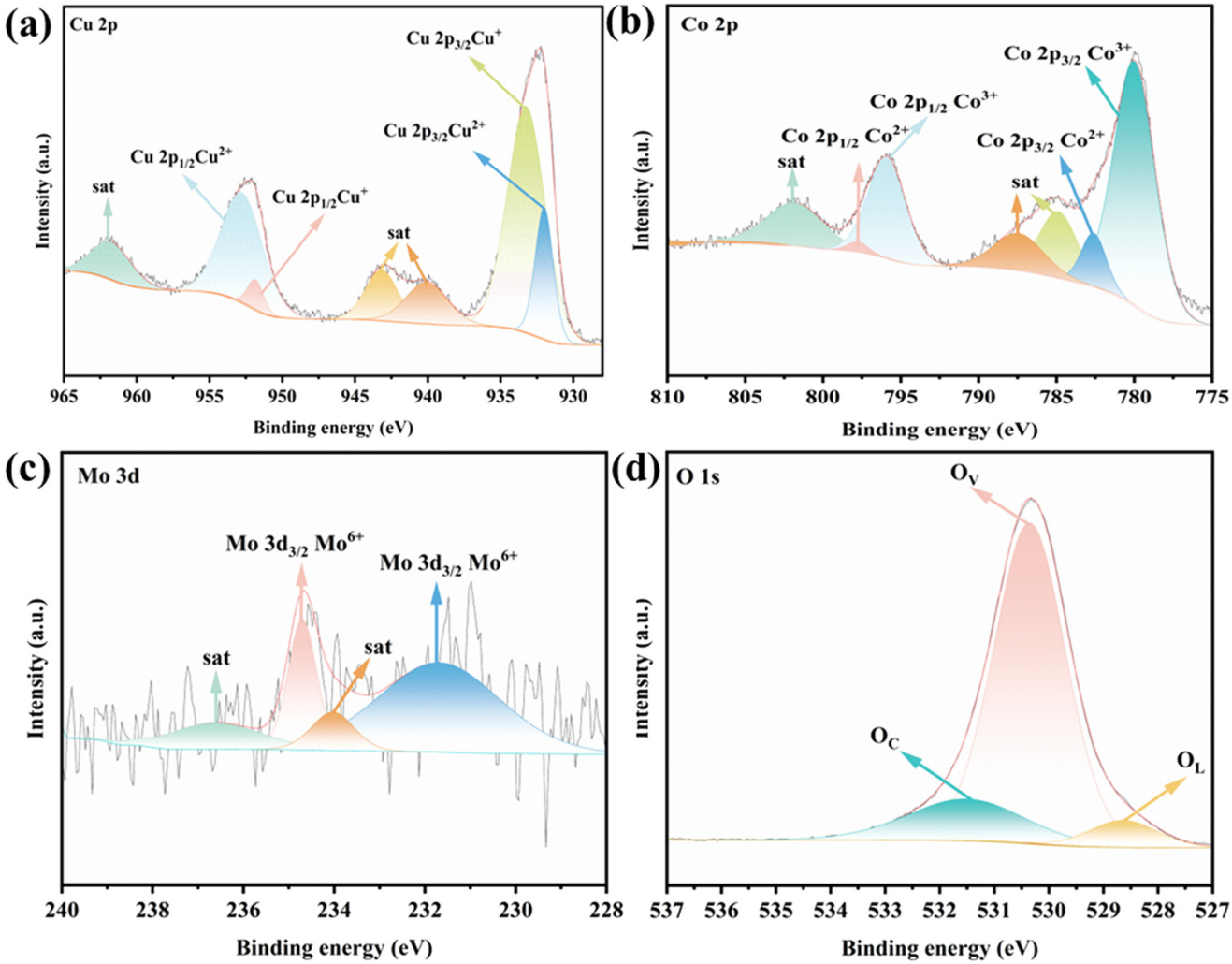

Fig. 9 (a) Mo 3d, (b) Co 2p, (c) Cu 2p, and (d) O 1s XPS spectra of $Cu_{0.95}Co_{2.05}O_4/MoO_3$/NF after 8 cycles of chronoamperometry at −0.25 V (*vs.* RHE) for 1.5 h.

952.71 and 951.79 eV were assigned to Cu^{2+} and Cu^{+} in the Cu $2p_{1/2}$ region, respectively. The intensity of the Cu^{+} peaks decreased relative to that of the Cu^{2+} peaks. Overall shifts in binding energies were observed for all the elements. During the pyrazine ECH process, both Cu^{+} and Co^{2+} were oxidized. The significant decrease in the O_L peak further confirms the reduction in Cu^{+} and Co^{2+}. Therefore, it is reasonable to infer that the main active components are Cu^{+}, Co^{2+}, and Mo^{6+}. Cu^{+} serves as the site for pyrazine adsorption and hydrogenation and is oxidized to Cu^{2+} during catalysis. Co^{2+} and Mo^{6+} promote the generation of H*. These findings are consistent with the electrochemical results discussed above.

Moreover, XRD analysis (Fig. S7) confirmed that the crystal structure of the catalyst essentially remained unchanged after 8 cycles, with no observable phase transformation or peak shift, further indicating its excellent structural stability. Overall shifts in binding energies were observed for all the elements. During the pyrazine ECH process, both Cu^{+} and Co^{2+} were oxidized. The significant decrease in the O_L peak further confirms the reduction in Cu^{+} and Co^{2+}. Therefore, it is reasonable to infer that the main active components are Cu^{+}, Co^{2+}, and Mo^{6+}. Cu^{+} serves as the site for pyrazine adsorption and hydrogenation and is oxidized to Cu^{2+} during catalysis. Co^{2+} and Mo^{6+} promote the generation of H*. These findings are consistent with the electrochemical results. Collectively, these results demonstrate the excellent long-term stability of the prepared $Cu_{0.95}Co_{2.05}O_4/MoO_3$/NF catalyst in terms of both catalytic performance and structural integrity.

3.3.5 Schematic of the ECH reaction. During the pyrazine ECH over $Cu_{0.95}Co_{2.05}O_4/MoO_3$/NF, the introduction of MoO_3 not only effectively stabilized the crystal structure of $Cu_{0.95}Co_{2.05}O_4$ but also optimized its electronic properties through electron modulation (Fig. 10). This synergistic effect enhances the overall catalytic performance. Structural regulation promotes the exposure of more active sites and significantly increases the overall catalytic activity

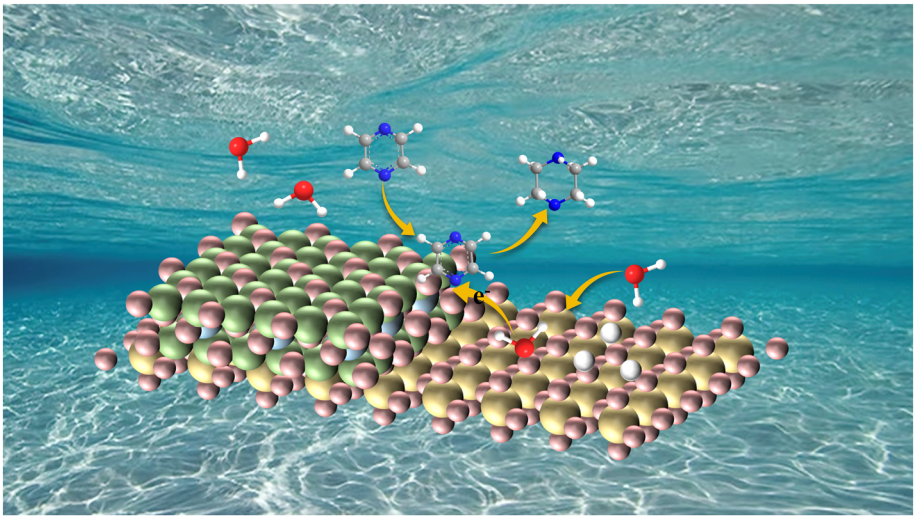

Fig. 10 Schematic of pyrazine hydrogenation with $Cu_{0.95}Co_{2.05}O_4/MoO_3$/NF.

at the heterojunction interface. This is specifically reflected in the simultaneous improvement in both the HER and the hydrogenation performance of organic molecules. In the pyrazine hydrogenation pathway, $Cu_{0.95}Co_{2.05}O_4/MoO_3$/NF has a bifunctional site characteristic. Co sites are responsible for H* generation, whereas Cu sites mainly adsorb pyrazine molecules. However, after the introduction of MoO_3 to form the $Cu_{0.95}Co_{2.05}O_4/MoO_3$/NF heterostructure, the catalytic mechanism is further optimized. Mo and Co jointly serve as active metals for the Volmer step, synergistically promoting the generation of abundant H*. Moreover, Cu sites continue to act as specific adsorption centers for pyrazine. Subsequently, *via* the HAT mechanism, the generated H* first migrates (spills over) to adjacent Cu sites. It then hydrogenates the adsorbed pyrazine to eventually form piperazine. After the reaction, the piperazine molecules desorb from the catalyst surface into the solution. This re-exposes the active sites, enabling the continuous progression of the catalytic cycle.

4 Conclusion

In this study, a self-supported $Cu_{0.95}Co_{2.05}O_4/MoO_3$/NF heterojunction electrocatalyst was successfully designed and fabricated for the efficient electrocatalytic hydrogenation of pyrazine to piperazine using water as the hydrogen source under mild alkaline conditions. A three-dimensional burr-like nanosheet heterointerface was constructed on nickel foam *via* a two-step method. XPS and HRTEM characterization confirmed the formation of a built-in electric field at the interface, arising from directional charge transfer from MoO_3 to $Cu_{0.95}Co_{2.05}O_4$ This electric field induces functional differentiation of the active sites: electron-rich Cu sites selectively adsorb and hydrogenate pyrazine, whereas electron-deficient Mo and Co sites promote water dissociation to generate H*. The spatially adjacent sites work synergistically through a surface spillover mechanism, effectively suppressing the competing hydrogen evolution reaction. Electrochemical tests demonstrated that the catalyst achieved a pyrazine conversion of >95% and a piperazine selectivity of >80% after 1.5 h of reaction at −0.25 V (*vs.* RHE), together with excellent cycling stability (8 cycles, 12 h). Practical scale-up experiments confirmed that the strategy of keeping the areal loading constant while linearly increasing the electrode area (from 1 cm × 1 cm to 7 cm × 7 cm) introduces no significant mass transport limitations or inhomogeneity, providing a feasible route for large-scale catalyst preparation. This study not only offers new materials and strategies for the mild, efficient, and low-cost electrocatalytic hydrogen storage of N-heterocyclic liquid organic hydrogen carriers but also provides important insights for the interfacial electronic engineering of non-noble metal heterojunction electrocatalysts.

Conflicts of interest

There are no conflicts of interest to declare.

Data availability

All study data are included in the article and/or supplementary information (SI) Appendix.

Supplementary information is available. See DOI: https://doi.org/10.1039/d6lf00079g.

Acknowledgements

This work was supported by the R&D Project of China Southern Power Grid Co Ltd (YNKJXM20240023).

References

1 N. D. Fita, I. Utu, M. D. Marcu, D. Pasculescu, I. O. Mila, F. G. Popescu, T. Lazar, A. M. Schiopu, F. Muresan-Grecu

and E. A. Cruceru, Global energy crisis and the risk of blackout: interdisciplinary analysis and perspectives on energy infrastructure and security, *Energies*, 2025, **18**, 4244, DOI: 10.3390/en18164244.

2 S. Singh, Energy crisis and climate change: Global concerns and their solutions, in *Energy: Crises, Challenges and Solutions*, John Wiley & Sons Ltd, 2021, pp. 1–17, DOI: 10.1002/9781119741503.ch1.

3 M. Farghali, A. I. Osman, I. M. A. Mohamed, Z. Chen, L. Chen, I. Ihara, P.-S. Yap and D. W. Rooney, Strategies to save energy in the context of the energy crisis: a review, *Environ. Chem. Lett.*, 2023, **21**, 2003–2039, DOI: 10.1007/s10311-023-01591-5.

4 L. Wang, W. Liu, H. Sun, L. Yang and L. Huang, Advancements and policy implications of green hydrogen production from renewable sources, *Energies*, 2024, **17**, 3548, DOI: 10.3390/en17143548.

5 S. P. Filippov and A. B. Yaroslavtsev, Hydrogen energy: development prospects and materials, *Russ. Chem. Rev.*, 2021, **90**, 627–643, DOI: 10.1070/RCR5014.

6 H. Barthelemy, M. Weber and F. Barbier, Hydrogen storage: recent improvements and industrial perspectives, *Int. J. Hydrogen Energy*, 2017, **42**, 7254–7262, DOI: 10.1016/j.ijhydene.2016.03.178.

7 L. Fang, X. Dong, H. Wang and M. Gong, Economic analysis of compressed gaseous hydrogen, liquid hydrogen, and cryo-compressed hydrogen storage methods for large-scale storage and transportation, *Int. J. Hydrogen Energy*, 2025, **162**, 150725, DOI: 10.1016/j.ijhydene.2025.150725.

8 M. R. Kalibek, A. D. Ospanova, B. Suleimenova, R. Soltan, T. Orazbek, A. M. Makhmet, K. S. Rafikova and N. Nuraje, Solid-state hydrogen storage materials, *Discover Nano*, 2024, **19**, 195, DOI: 10.1186/s11671-024-04137-y.

9 C. Lang, Y. Jia and X. Yao, Recent advances in liquid-phase chemical hydrogen storage, *Energy Storage Mater.*, 2020, **26**, 290–312, DOI: 10.1016/j.ensm.2020.01.010.

10 H. K. Thakkar, K. H. Modi, K. K. Joshi, G. Bhadu, S. Siraj, P. Sahatiya, P. M. Pataniya and C. Sumesh, Vertically oriented FeNiO nanosheet array for urea and water electrolysis at industrial-scale current density, *ACS Sustainable Chem. Eng.*, 2024, **12**, 8340–8352, DOI: 10.1021/acssuschemeng.4c00591.

11 N. A. Trivedi, P. J. Sharma, K. K. Joshi, V. Patel, C. Sumesh and P. M. Pataniya, ReS_2/CoS heterostructure catalysts for electrochemical application in hydrogen evolution and supercapacitor, *Int. J. Hydrogen Energy*, 2024, **61**, 1212–1219, DOI: 10.1016/j.ijhydene.2024.03.050.

12 S. V. Chauhan, K. K. Joshi, P. M. Pataniya and C. K. Sumesh, Advancing industrial rate current density in water electrolysis for green hydrogen production: catalyst development, benchmarking, and best practices, *Sustainable Energy Fuels*, 2025, **9**, 3550–3576, DOI: 10.1039/D5SE00262A.

13 H. Jorschick, P. Preuster, A. Bösmann and P. Wasserscheid, Hydrogenation of aromatic and heteroaromatic compounds–a key process for future logistics of green hydrogen using liquid organic hydrogen carrier systems, *Sustainable Energy Fuels*, 2021, **5**, 1311–1346, DOI: 10.1039/D0SE01369B.

14 Y. Sekine and T. Higo, Recent trends on the dehydrogenation catalysis of liquid organic hydrogen carrier (LOHC): a review, *Top. Catal.*, 2021, **64**, 470–480, DOI: 10.1007/s11244-021-01452-x.

15 N. T. Padmanabhan, L. Clarizia and P. Ganguly, Advancing hydrogen storage: critical insights to potentials, challenges, and pathways to sustainability, *Curr. Opin. Chem. Eng.*, 2025, **48**, 101135, DOI: 10.1016/j.coche.2025.101135.

16 K. H. Modi, P. M. Pataniya, S. Siraj, P. Sahatiya, V. Patel and C. K. Sumesh, Synergistic effect from Ni^{2+} ions with SnS for all solid-state type symmetric supercapacitor, *J. Energy Storage*, 2023, **63**, 107040, DOI: 10.1016/j.est.2023.107040.

17 H. Li, X. Zhang, C. Zhang, Z. Ding and X. Jin, Application and analysis of liquid organic hydrogen carrier (LOHC) technology in practical projects, *Energies*, 2024, **17**, 1940, DOI: 10.3390/en17081940.

18 K. C. Tan, T. He, Y. S. Chua and P. Chen, Recent advances of catalysis in the hydrogenation and dehydrogenation of N-heterocycles for hydrogen storage, *J. Phys. Chem. C*, 2021, **125**, 18553–18566, DOI: 10.1021/acs.jpcc.1c04783.

19 X. Zhao, X. Kong, G. Li, Y. Zhao, Z. Jia, F. He, P. Yang, K. Ge, M. Zhang and Z. Liu, Ru-based catalysts for hydrogenation of N-ethylcarbazole: Progress and prospects, *Fuel*, 2024, **360**, 130605, DOI: 10.1016/j.fuel.2023.130605.

20 S. Guo, Y. Wu, C. Wang, Y. Gao, M. Li, B. Zhang and C. Liu, Electrocatalytic hydrogenation of quinolines with water over a fluorine-modified cobalt catalyst, *Nat. Commun.*, 2022, **13**, 5297, DOI: 10.1038/s41467-022-32933-6.

21 D. Sharma, P. Choudhary, P. Mittal, S. Kumar, A. Gouda and V. Krishnan, Nanoarchitectonics of non-noble-metal-based heterogeneous catalysts for transfer hydrogenation reactions: detailed insights on different hydrogen sources, *ACS Catal.*, 2024, **14**, 4211–4248, DOI: 10.1021/acscatal.3c05844.

22 C. Liu, Y. Wu, B. Zhao and B. Zhang, Designed nanomaterials for electrocatalytic organic hydrogenation using water as the hydrogen source, *Acc. Chem. Res.*, 2023, **56**, 1872–1883, DOI: 10.1021/acs.accounts.3c00192.

23 Y. Zhao, J. Xu, K. Huang, W. Ge, Z. Liu, C. Lian, H. Liu, H. Jiang and C. Li, Dopant-and surfactant-tuned electrode–electrolyte interface enabling efficient alkynol semi-hydrogenation, *J. Am. Chem. Soc.*, 2023, **145**, 6516–6525, DOI: 10.1021/jacs.3c00565.

24 S. Kolb and D. B. Werz, Site-selective hydrogenation/deuteration of benzylic olefins enabled by electroreduction using water, *Chem. – Eur. J.*, 2023, **29**, e202300849, DOI: 10.1002/chem.202300849.

25 P. Zhang and H. He, Rational rope-like $CuCo_2O_4$ nanosheets directly on Ni foam as multifunctional electrodes for supercapacitor and oxygen evolution reaction, *J. Alloys Compd.*, 2020, **826**, 153993, DOI: 10.1016/j.jallcom.2020.153993.

26 S. Wang, S. Zhang, S. Liu, Z. Zhang, Y. Tan and K. Liang, Highly selective interconversion of quinoxaline and 1, 2, 3, 4-tetrahydroquinoxaline over a spinel $CuCo_2O_4$ electrocatalyst supported by Ni foam, *Chem. Phys. Lett.*, 2024, **856**, 141638, DOI: 10.1016/j.cplett.2024.141638.

27 X. Liu, X. Cheng, H. Zhao, P. Liu and Y.-Q. Wang, $CuCo_2O_4$/CuO heterostructure with oxygen vacancies induced by plasma for electrocatalytic nitrate reduction to ammonia, *Inorg. Chem.*, 2024, **63**, 14093–14102, DOI: 10.1021/acs.inorgchem.4c01924.

28 M. Tian, J. Wang, L. Li, X. Yu, X. Zhang, Z. Lu, W. Shang and X. Yang, Built-in electric field engineering in $CuCo_2O_4$-CuO heterostructures for enhanced ammonia borane hydrolytic dehydrogenation, *J. Alloys Compd.*, 2025, **1036**, 181975, DOI: 10.1016/j.jallcom.2025.181975.

29 M. Liu, J. Wang, Q. Tian, Y. Liu, P. Li, W. Li, N. Cai, Y. Xue, W. Chen and F. Yu, Mo-doped Cu/Co hybrid oxide nanoarrays: an enhanced electrocatalytic performance for the hydrogen evolution reaction, *ChemElectroChem*, 2019, **6**, 1738–1744, DOI: 10.1002/celc.201801790.

30 T. Falk, E. Budiyanto, M. Dreyer, J. Büker, C. Weidenthaler, M. Behrens, H. Tüysüz, M. Muhler and B. Peng, Doping of nanostructured Co_3O_4 with Cr, Mn, Fe, Ni, and Cu for the selective oxidation of 2-propanol, *ACS Appl. Nano Mater.*, 2022, **5**, 17783–17794, DOI: 10.1021/acsanm.2c03757.

31 L. Ding, L. Wang, J. Gao, T. Yan, H. Li, J. Mao, F. Song, S. Fedotov, L.-Y. Chang, N. Li, Y. Su, T. Liu and L. Zhang, Facile Zn^{2+} desolvation enabled by local coordination engineering for long-cycling aqueous zinc-ion batteries, *Adv. Funct. Mater.*, 2023, **33**, 2301648, DOI: 10.1002/adfm.202301648.

32 W. Zhang, C. Li, J.-Y. Ji, Z. Niu, H. Gu, B. F. Abrahams and J.-P. Lang, Tailorable carbon cloth electrodes covered with heterostructured Co/CoO/CoN interfaces for scalable electrocatalytic overall water splitting, *Chem. Eng. J.*, 2023, **461**, 141937, DOI: 10.1016/j.cej.2023.141937.

33 M. Wang, H. Du, H. Zhao, Y. Cao, R. Dong, H. Wang and H. Hou, Dual promoting effects of hereditary Mn doping and oxygen vacancies on porous $CuCo_2O_4$ for electrocatalytic oxygen generation, *ACS Sustainable Chem. Eng.*, 2023, **11**, 9478–9488, DOI: 10.1021/acssuschemeng.3c01839.

34 R. P. Patel, P. M. Pataniya, S. Siraj, P. Sahatiya and C. Sumesh, Simultaneous production of green hydrogen and decontamination of dye wastewater using WSe_2-CuO/graphite electrochemical cell, *Int. J. Hydrogen Energy*, 2024, **55**, 815–827, DOI: 10.1016/j.ijhydene.2023.11.246.

35 M. Tian, B. Hui, T. Jia, X. Chen, L. Li, X. Yu, X. Zhang, Z. Lu and X. Yang, Anion modulation enhances the internal electric field of $CuCo_2O_4$ to improve the catalysis in ammonia borane hydrolysis, *J. Colloid Interface Sci.*, 2025, **683**, 236–246, DOI: 10.1016/j.jcis.2024.12.206.

36 M. Yang, Z. Ye, M. A. Iqbal, H. Liang and Y.-J. Zeng, Progress on two-dimensional binary oxide materials, *Nanoscale*, 2022, **14**, 9576–9608, DOI: 10.1039/D2NR01076C.

37 S. A. Adewinbi, B. A. Taleatu, R. A. Busari, V. M. Maphiri, K. O. Oyedotun and N. Manyala, Synthesis and electrochemical characterization of pseudocapacitive α-MoO_3 thin film as transparent electrode material in optoelectronic and energy storage devices, *Mater. Chem. Phys.*, 2021, **264**, 124468, DOI: 10.1016/j.matchemphys.2021.124468.

38 V. Prajapati, A. Shah, D. N. Srivastava, P. M. Pataniya and C. K. Sumesh, Scalable synthesis of binder-free MXene based electrode for green hydrogen production, *J. Mater. Sci.: Mater. Electron.*, 2024, **35**, 580, DOI: 10.1007/s10854-024-12332-x.

39 P. Mishra, P. Sudarsanam, D. M. Mahapatra, A. Elmekawy, D. Pant and L. Singh, Progressions in cathodic catalysts for oxygen reduction and hydrogen evolution in bioelectrochemical systems: molybdenum as the next-generation catalyst, *Catal. Rev.: Sci. Eng.*, 2023, **65**, 986–1078, DOI: 10.1080/01614940.2021.2003085.

40 Z. Hou, D. Yang, Y. Xin, H. Huang, X. Hu, Y. Guo, S. Wu and L. Hu, In situ coupled MoO_3 with CoP/rGO to construct three-dimensional self-supported catalyst for highly efficient alkaline hydrogen evolution reaction, *J. Mater. Sci. Technol.*, 2022, **104**, 194–201, DOI: 10.1016/j.jmst.2021.06.047.

41 H. Jiang, Y. Yu, X. Duan, P. Chen, S. Wang, X. Qiu, L. Ye and X. Tu, Heterostructured MoO_3 anchored defect-rich NiFe-LDH/NF as a robust self-supporting electrocatalyst for overall water splitting, *Small*, 2023, **20**, 2307797, DOI: 10.1002/smll.202307797.

42 N. Diyali, S. Diyali, M. Chettri, S. Saha, S. K. Agrawalla, H. Bagdwal, C. S. Purohit, M. Singh and B. Biswas, Operando electro-oxidation reconstitution of a newly designed 2D Co (II)-MOF on nickel foam to cobalt oxyhydroxide nanosheets towards energy sustainability: a holy grail in electrocatalytic water splitting, *ACS Appl. Mater. Interfaces*, 2025, **17**, 9351–9363, DOI: 10.1021/acsami.4c20152.

43 C. Huang, J. Nie, Z. Xu, X. Zhang, J. Tang, B. Wang, J. Huang, C. Du and J. Chen, One-step hydrothermal synthesized 3D P-MoO_3/FeCo LDH heterostructure electrocatalysts on Ni foam for high-efficiency oxygen evolution electrocatalysis, *Int. J. Hydrogen Energy*, 2021, **46**, 12992–13000, DOI: 10.1016/j.ijhydene.2021.01.145.

44 W. Abbas, M. Irfan, M. Babur, M. E. Mazhar, J. Ahmad, K. A. Rao, S. Haider, H. Ali, M. Imtiaz and M. Imran, Synergistic $CuCo_2O_4$/MWCNT nanocomposites: advanced electrode materials for energy storage and catalysis applications, *J. Mater. Sci.: Mater. Eng.*, 2025, **20**, 96, DOI: 10.1186/s40712-025-00313-9.

45 Y. Pan, H. Li, J. Xiong, Y. Yu, H. Du, S. Li, Z. Wu, S. Li, J. Lai and L. Wang, Protecting the state of Cu clusters and nanoconfinement engineering over hollow mesoporous carbon spheres for electrocatalytical C-C coupling, *Appl. Catal., B*, 2022, **306**, 121111, DOI: 10.1016/j.apcatb.2022.121111.

46 Z. Zhong, J. Yan, B. Chen, Q. Zhang, Y. Zhu, S. Xu, A. Xie and S. Luo, Effect of different preparation technologies of $CuCo_2O_4$ on electrocatalytic activity for oxidation of alcohols, *J. Solid State Chem.*, 2024, **332**, 124574, DOI: 10.1016/j.jssc.2024.124574.

47 G. Zhao, J. Wang, P. Jiang, D. Liu, K. Huang, A. T. Kuvarega, B. B. Mamba and J. Gui, Three-dimensional cross-nanosheets structured $CuCo_2O_4$ catalyst for highly efficient

toluene oxidation, *Appl. Surf. Sci.*, 2025, **705**, 163522, DOI: 10.1016/j.apsusc.2025.163522.

48 H. Wang, X. Du and X. Zhang, Controlled synthesis of $NiSe_2$-$NiMoO_4$-MoO_3 material on nickel foam as an efficient hydrogen evolution reaction catalyst in seawater and urea electrolytes, *Sustainable Mater. Technol.*, 2024, **42**, e01158, DOI: 10.1016/j.susmat.2024.e01158.